High Quality Co-Sputtering AlScN Thin Films for Piezoelectric Lamb-Wave Resonators

Shuai Shao, Zhifang Luo, *Student Member, IEEE*, Yuan Lu, Andrea Mazzalai, Carlo Tosi, and Tao Wu, *Senior Member, IEEE*

***Abstract*— Doped AlN thin films, especially high Sc-ratio AlScN film, have been reported to significantly improve the piezoelectric properties and draw attention for high performance resonators, transducers and integrated ferroelectric applications. However, many demonstrated devices were limited by poor film stress control, abnormal oriented grains and lack of a good etching profile. Compared to costly single alloy target, co-sputtered AlScN films can benefit customized doping concentrations and provide a unique solution for high Sc-ratio AlScN film quality and device studies. In this work, the optimized co-sputtering deposition and ICP etching processes of 500 nm AlScN thin film were developed and released AlScN Lamb-wave resonators were demonstrated. The influence of stress control by changing N_2 process gas on the crystalline orientation, abnormal orientation grains, film roughness and piezoelectric property of AlScN thin films were discussed in detail. The AlScN film with a high Sc content requires a lower deposition pressure to obtain good crystalline quality. $Al_{0.85}Sc_{0.15}N$ thin films with FWHM of 1.75°, an average stress of −14.5 MPa and a stress range of 156 MPa were obtained. 130 nm/min etching rate and 77° sidewall profile were achieved by optimized ICP etching of $Al_{0.78}Sc_{0.22}N$ film. Lamb-wave resonators were fabricated based on both $Al_{0.78}Sc_{0.22}N$ and $Al_{0.85}Sc_{0.15}N$ thin films, achieving a quality factor of over 1000 at resonant frequency of approximately 300 MHz. The electromechanical coupling coefficients were improved by 152% and 80% compared to pure AlN devices. [2021-0210]**

***Index Terms*— AlScN, stress control, co-sputter, ICP etch, Lamb-wave resonator.**

I. Introduction

With the wide application of resonators and actuators in RF devices and sensors, chip-scale piezoelectric devices have become an attractive technology [1]–[4]. The emerging 5G application requires high-performance filters with wide bandwidth, low insertion loss and high power handling capacity below 6 GHz for wireless communication devices [5]. For example, the n78 bands in 5G demand a bandwidth of 500 MHz at 3800 MHz, which means the fractional bandwidth should be above 10%. The acoustic resonance devices comprising the filters require a large quality factor, high electromechanical coupling coefficient (k_t^2) and high-power handling capability. Because of its high phase velocity, strong polarity, low temperature frequency coefficient (TCF), and post-CMOS compatibility, aluminum nitride (AlN) thin film is one of the preferred piezoelectric materials for Radio Frequency (RF) communication application [6]. However, compared with other piezoelectric materials such as lithium niobate, lithium tantalate and PZT, the d_{33} of AlN is only around 5.5 pC/N [7], [8]. The low piezoelectric constant of AlN limits the maximum k_t^2 of Film Bulk Acoustic Resonator (FBAR) to approximately 7% [9], [10] and Contour Mode Resonator (CMR) to approximately 3% [9]. To further improve the k_t^2, Cross-Sectional Lamé Mode (CLMR) and Two-Dimensional-Resonant-Rods (2DDRs) using a combination of d_{31} and d_{33} were demonstrated increasing to 5% and 9%, respectively [11]–[13]. Moreover, the piezoelectric transducers typically require a larger d_{33} and d_{31} for sensing and actuating applications. It has been reported that the piezoelectric properties can be significantly enhanced by doping scandium (Sc) into aluminum nitride [14], [15]. The k_t^2 of Lamb-wave resonators and 2DDRs were also increased remarkably as expected [16], [17]. The piezoelectric constant d_{33} can be promoted to more than 25 pC/N, making AlScN film a promising material for future mobile communication and transducer applications. However, as a metastable hexagonal phase, AlScN has more stringent requirements on deposition process conditions than pure AlN [18].

AlScN thin film growth and dry etching are two major challenges compared to conventional pure AlN film [19]. During AlScN growth processes, good crystalline orientation needs to be obtained for the performance of the devices. In addition, the film stress significantly impacts the yield and the performance of the released structures due to the extensive use of suspended structures in piezoelectric MEMS resonators and transducers [20]. AlScN thin film has been reported to be successfully grown epitaxially using metal-organic chemical vapor deposition (MOCVD), molecular beam epitaxy (MBE)

Manuscript received October 1, 2021; revised February 13, 2022; accepted March 12, 2022. Date of publication April 7, 2022; date of current version June 2, 2022. This work was supported in part by the National Natural Science Foundation of China under Grant 61874073, in part by the Natural Science Foundation of Shanghai under Grant 19ZR1477000, and in part by the Lingang Laboratory under Grant LG-QS-202202-05. Subject Editor S. Gong. *(Corresponding authors: Shuai Shao; Tao Wu.)*

Shuai Shao, Zhifang Luo, and Tao Wu are with the School of Information Science and Technology, ShanghaiTech University, Shanghai 201210, China, also with the Shanghai Institute of Microsystem and Information Technology, Shanghai 200050, China, and also with the School of Electronic, Electrical and Communication Engineering, University of Chinese Academy of Sciences, Shijingshan, Beijing 100049, China (e-mail: shaoshuai@shanghaitech.edu.cn; luozhf@shanghaitech.edu.cn; wutao@shanghaitech.edu.cn).

Yuan Lu, Andrea Mazzalai, and Carlo Tosi are with Evatec AG, 9477 Trüebbach, Switzerland.

Color versions of one or more figures in this article are available at https://doi.org/10.1109/JMEMS.2022.3161055.

Digital Object Identifier 10.1109/JMEMS.2022.3161055

1057-7157 © 2022 IEEE. Personal use is permitted, but republication/redistribution requires IEEE permission.
See https://www.ieee.org/publications/rights/index.html for more information.

Authorized licensed use limited to: ShanghaiTech University. Downloaded on June 26,2022 at 07:31:59 UTC from IEEE Xplore. Restrictions apply.

and magnetron sputtering deposition [21]–[24]. However, due to the slow growth rate, epitaxial growth is more suitable as a thin buffer layer for lattice matching in semiconductor devices rather than sub-micron MEMS applications [21]. Moreover, the epitaxial growth of sub-micron thickness could easily cause cracks after structure release due to excessive stress. Therefore, the low cost, relatively high deposition rate and stress control capability of reactive magnetron sputtering become the most promising growth process [25], [26]. The stress control on piezoelectric constants and device performance has been discussed [27], [28]. The film quality much influences the piezoelectric constant, and a larger piezoelectric constant can be achieved in the well deposited film. A better stress-controlled film provides a larger design space for better performance, such as laterally vibrating resonators with thinner anchor width. Controlling deposition pressure, substrate or target bias and magnetron source distribution are the main stress tuning methods [25], [28]–[31]. This work focuses on the effect of pure N_2 on crystalline orientation, the number of abnormal orientation grains (AOGs), piezoelectric constant, and roughness. Inductively coupled plasma (ICP) etching defines the release trench and reflection boundaries in the resonator fabrication. However, it has been reported that the etching rate of AlScN films decreases significantly, compared to AlN films [32], [33]. As the etching rate and the selectivity of the mask decrease, the angle of the etching profile also deteriorates, resulting in inefficient reflection boundary and parasitic modes.

Herein, we report optimized magnetron co-sputtering and ICP etching process of 500 nm thick AlScN film and obtain Lamb-wave resonators based on 15.5% and 22.5% two Sc concentrations. The resonators operate at 310.8 MHz and 292.5 MHz, achieving k_t^2 of 3.7% and 5.1%, respectively, as well as quality factors of over 1000. We have verified the different formation energy correlating to the process window needed for specific Sc concentrations by setting the growth parameters. Through the X-ray diffraction (XRD) measurement and analysis of the AlScN, the relative longitudinal piezoelectric constant can be directly related to the FWHM of 0002 AlScN film. Moreover, even at the same Sc concentration, the c lattice parameter is found to shift by setting different N_2 flow/pressure. The number of AOGs is independent of the FWHM. AlScN thin films with both low stress and good crystal quality were obtained. By optimizing the ICP etching process, an etching rate of 130 nm/min and a profile of 77° were achieved. Finally, Lamb-wave resonators with floating bottom electrodes based on 15.5% and 22.5% AlScN were fabricated and show the great potential of high Sc-ratio AlScN thin films.

II. Design of Lamb-Wave Resonators Based on AlScN

Thanks to the high phase velocity, strong polarity, and the capability to be integrated with the post-CMOS process, aluminum nitride-based resonators are now widely used in sensors and RF filters. FBAR has become a commercial success case due to the high quality factor (Q) and k_t^2. However, the bulk acoustic wave mode limits the ability of FBAR to modulate the frequency using lithography. Lamb-wave resonators just solve this problem and become a promising single-chip solution for a wide frequency range [9], [34]. Due to the low piezoelectric constant of pure AlN, the k_t^2 of the Lamb-wave resonator is relatively low, and AlScN compensates for this deficiency.

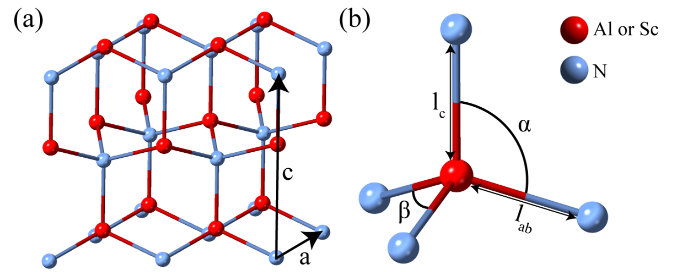

Fig. 1. (a) AlScN with hexagonal wurtzite structure, where red color represents Al or Sc atoms, blue color represents N atoms. (b) Tetrahedral structure with bond angle.

TABLE I
Material Parameters of AlScN [18], [31]

Parameters	AlN	$Al_{0.85}Sc_{0.15}N$	$Al_{0.78}Sc_{0.22}N$
c_{11}^E [GPa]	410.2	366.2	347.7
c_{12}^E [GPa]	142.4	142.9	144.3
c_{13}^E [GPa]	110.1	124.0	129.6
c_{33}^E [GPa]	385.0	310.8	275.3
c_{44}^E [GPa]	122.9	112.4	109.4
e_{15} [C/m^2]	-0.39	-0.35	-0.33
e_{31} [C/m^2]	-0.63	-0.69	-0.71
e_{33} [C/m^2]	1.46	1.72	1.94
$\varepsilon_{33}^{eff}/\varepsilon_0$	9.0	13.2	16.1
ρ [kg/m^3]	3230	3272	3293
a [Å]	3.13	3.20	3.23
c [Å]	5.02	5.04	5.05

Figures 1a and b show that Sc replaces Al atoms in the hexagonal wurtzite AlN structure. From the result of the elastic constant C, C_{11} and C_{33} are decreasing as in the higher Sc concentration as shown in Table I. The reduction in the elastic coefficient leads to a decrease in the wave velocity of both longitudinal and transverse waves compared to AlN. To compare the bond length of a/c and the bond angle α and β: the higher Sc incorporation brings larger bond length in a and c and the larger bond angle of β [35]. That is the reason for the decline in elastic constant c as the Sc content increases, but all features also lead to a higher dipole moment, especially the force is along the c axis, causing a higher piezoelectric constant d_{33}. From this statement, we could expect a higher piezoelectric response of the AlScN-based device. However, the lower elastic constant could also decrease the quality factor of the device. The good piezoelectric effect of AlScN needs to be optimized for the performance improvement of the device.

A few works have demonstrated resonator performance benefiting from AlScN thin films [16], [36]–[42]. In this work, the design of the Lamb-wave resonator, as shown in Figure 2a, consists of an AlScN plate, IDT, floating electrode and anchor. The vertical electric field between the IDT and the floating electrode excites the S0 mode by d_{31} and d_{33}. The resonant

Authorized licensed use limited to: ShanghaiTech University. Downloaded on June 26,2022 at 07:31:59 UTC from IEEE Xplore. Restrictions apply.

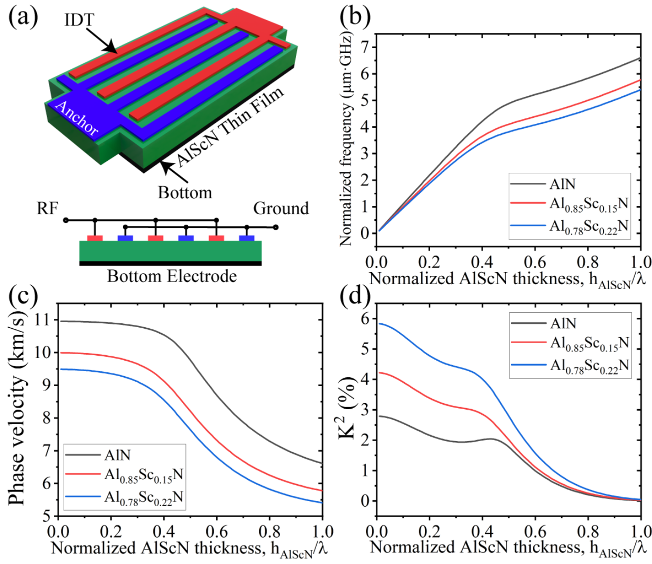

Fig. 2. (a) Illustrations of the Lamb-wave resonator with floating bottom electrode. (b) Normalized frequency, (c) Phase velocity dispersion curves and (d) S0 mode k^2 with AlN, $Al_{0.78}Sc_{0.22}N$ and $Al_{0.85}Sc_{0.15}N$.

frequency of the Lamb-wave resonator is determined by the following equation

$$f_r = \sqrt{\frac{E_{eq}}{\rho_{eq}}} \cdot \frac{1}{2W} \tag{1}$$

where E_{eq} and ρ_{eq} are the equivalent elasticity and density of the stack, respectively, and W is the pitch between electrodes. To evaluate the S0 mode dispersion characteristics of the intrinsic coupling coefficients (K^2) based on $Al_{0.85}Sc_{0.15}N$ and $Al_{0.78}Sc_{0.22}N$, the difference in phase velocity between the free surface v_0 and the metalized surface v_m were used [14].

$$K^2 = \frac{v_0^2 - v_m^2}{v_0^2} \tag{2}$$

In the finite element simulation, periodic boundaries are applied on both sides of the AlScN flat plate to obtain the resonant frequencies of the Lamb-wave eigenmodes to calculate the phase velocities. The metalized surface v_m is obtained by applying the potential boundary.

Figure 2b gives the normalized frequency versus wavenumber, where Sc doping reduces the resonant frequency of the S0 Lamb-wave for the same dimensions (h/λ). Figure 2c shows the dispersion of the phase velocities of AlN, $Al_{0.85}Sc_{0.15}N$ and $Al_{0.78}Sc_{0.22}N$ in the S0 mode. Sc doping does not change the trend of the phase velocity curve. The higher the doping concentration, the lower the phase velocity of the film due to the lower elasticity coefficient. The material parameters of $Al_{0.85}Sc_{0.15}N$ and $Al_{0.78}Sc_{0.22}N$ based on the ab-initio equations were reported in [43], [44]. 15% and 22% Sc doping cause 8.9% and 13.4% decrease in the S0 mode phase velocity, respectively. Figure 2d shows the dispersion characteristics of the S0 mode Lamb-wave in AlScN films through finite element simulation. The dispersion properties demonstrate that the k^2 are increased by 52.8% and 110% with $Al_{0.85}Sc_{0.15}N$ and $Al_{0.78}Sc_{0.22}N$ when h/λ is 0.2. Meanwhile, it is also worth noting that the deterioration of the thermal conductivity due to high Sc doping has been reported [45], resulting in a power handling challenge. The Sc ratio needs to be optimized to achieve a balance between piezoelectric constants and power handling.

TABLE II

OVERVIEW OF THE DEPOSITION PARAMETERS

Parameters	Value	Parameters	Value
Aluminum target power	1000 W	Target to substrate distance	38 mm
Scandium target power	300 W/450 W	N_2 flow	16-30 sccm
Base pressure	$<5\times10^{-7}$ mbar	Temperature	350 °C

III. AlScN THIN FILM GROWTH

AlScN film magnetron DC-pulsed co-sputtering system utilizes two 4-inch Al and Sc targets. The pulsed DC power of each target can be independently controlled in addition to conventional substrate bias as well as chuck height (distance between the substrate and the targets). Detailed deposition parameters are shown in Table II. 500 nm thick AlScN thin films were deposited on 8-inch silicon wafers (100) using a pulsed DC magnetron reactive co-sputtering system in the EVATEC CLUSTERLINE® 200 MSQ multi-source system. The base pressure of the chamber before the deposition was evacuated to less than 1×10^{-7} mbar. The wafer surface was cleaned for 1 min by argon ICP etching to remove the natural oxide layer and improve the nucleation conditions of AlScN films. All sputtering deposition was at 350 °C. The power of Al target was kept constant at 1000 W. By changing the power of Sc target, AlScN thin films with different concentrations were obtained. The powers of Sc target were 300 W and 450 W corresponding to the Sc concentration of 15.5% and 22.5%, respectively.

In order to evaluate the influence of process pressure on the piezoelectric properties of the AlScN thin film, two sets of experiments were conducted. Firstly, to compare the impact of N_2/Ar mixture and pure N_2 on the film quality, the gas in one group was N_2 = 24 sccm and the other was N_2/Ar = 16/8 sccm, keeping the total gas flow the same. Secondly, to analyze the effect of pressure at different Sc concentrations, the powers of Sc target were set at 300 W and 450 W, respectively, and N_2 flow was varied from 16-30 sccm. To investigate the mechanism of pressure effects on piezoelectric constant, XRD, grain size, AOGs and surface morphology were characterized. Finally, the trend of pressure on stress was evaluated to obtain a film suitable for device fabrication.

We investigated the influence of N_2/Ar mixture and pure N_2 on the film quality, in which the gas was set at N_2 = 24 sccm and N_2/Ar = 16/8 sccm with $Al_{0.85}Sc_{0.15}N$ and $Al_{0.78}Sc_{0.22}N$, respectively. The rocking curve FWHM of $Al_{0.85}Sc_{0.15}N$ decreases from 1.75° for N_2 = 24 sccm to 2.30° for N_2/Ar = 16/8 sccm. While the rocking curve FWHM of

Authorized licensed use limited to: ShanghaiTech University. Downloaded on June 26,2022 at 07:31:59 UTC from IEEE Xplore. Restrictions apply.

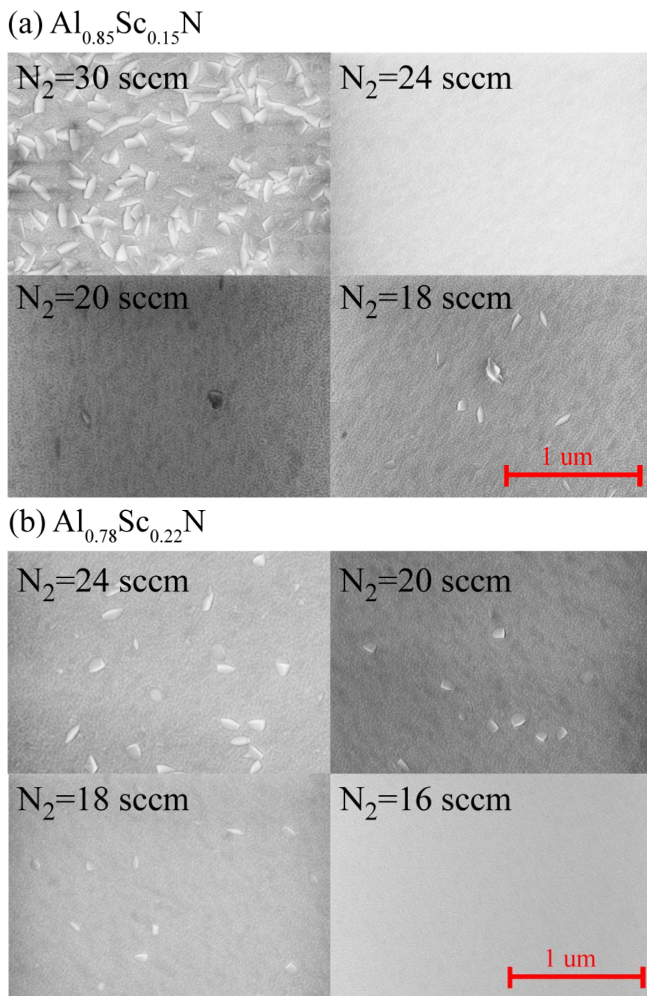

Fig. 3. SEM images of (a) $Al_{0.85}Sc_{0.15}N$ and (b) $Al_{0.78}Sc_{0.22}N$ thin films with different N_2 flow.

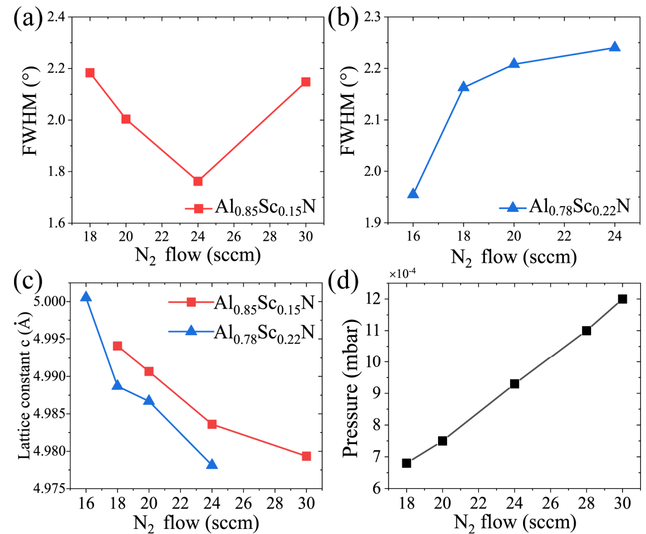

Fig. 4. (a) FWHM of $Al_{0.85}Sc_{0.15}N$ 0002 rocking-curve as a function of N_2 from 18 sccm to 30 sccm, insert is the rocking curve under 24 sccm N_2 flow. (b) FWHM of $Al_{0.78}Sc_{0.22}N$ 0002 rocking-curve as a function of N_2 from 16 sccm to 24 sccm. (c) The effect of gas flow rate on the lattice constant c of films with different concentrations. (d) N_2 gas flow rate versus pressure in the chamber.

$Al_{0.78}Sc_{0.22}N$ decreases from 2.24° for $N_2 = 24$ sccm to 2.54° for $N_2/Ar = 16/8$ sccm. This trend is similar to other reported work [24]. Therefore, pure N_2 gas was used in all AlScN depositions.

In order to analyze the effect of pressure at different Sc concentrations, the powers of Sc target were set at 300 W and 450 W, and N_2 flow was varied from 16 to 30 sccm. Figures 3a and b showed the SEM top view of the $Al_{0.85}Sc_{0.15}N$ and $Al_{0.78}Sc_{0.22}N$ (indicate wafer center) and the XRD FWHM of the corresponding sample. In the $Al_{0.85}Sc_{0.15}N$ side (Figure 3a and Figure 4a), massive AOGs are found and the XRD FWHM AlScN 0002 reached 2.2° at the center. With a decrease of the N_2 process flow to 24 sccm, the SEM image shows the complete disappearance of the AOGs. While the XRD FWHM AlScN 0002 both wafer center and edge achieved 1.75°/2.05°, indicating the better crystalline quality by decreasing the N_2 flow to 24 sccm. By further decreasing the N_2 flow to 20 and 18 sccm, a slight increase of the AOGs could be observed by SEM images. Similar to the other samples in this group, an increase of the XRD FWHM is thus also observed. Surprisingly the FWHM XRD of the 18 sccm and 30 sccm is very close, however, the SEM indicates totally different AOGs distribution between these two samples. Due to the existence of abnormally oriented grains, the quality of AlScN cannot be judged solely by the FWHM of the rocking curve. The intensity of ion bombardment has a dramatic effect on the growth of AOGs. Therefore, SEM or AFM and other surface morphology methods should be performed. XRD pattern or rocking curve is used for further crystalline quality comparison.

In the $Al_{0.78}Sc_{0.22}N$ side (Figure 3b and Figure 4b), the sample sputtered under 24 sccm has slightly AOGs distributed cross the wafer and the XRD FWHM AlScN 0002 reached 2.2°/2.45° for wafer center and edge. For the N_2 flow of 24 sccm, higher Sc incorporation leads to higher XRD FWHM when using the same sputtering parameter and thickness. With more tuning knobs, such as RF bias, chuck height, etc., in commercial PVD tools using alloy target, the sputtered AlScN film crystal quality can be further optimized. In the $Al_{0.78}Sc_{0.22}N$ sample group, the decrease of N_2 flow leads to a decrease of the AOGs density and thus a decreased value in XRD FWHM. However, different from the trend of varying N_2 flow in $Al_{0.85}Sc_{0.15}N$, for $Al_{0.78}Sc_{0.22}N$ the higher crystalline quality prefers lower N_2 flow/higher vacuum level. The best crystalline quality is obtained by $N_2 = 16$ sccm and the XRD rocking curve FWHM reached 1.93°/2.25° at wafer center/edge, respectively. Rassay *et al.* [46] reported an $Al_{0.78}Sc_{0.22}N$ thin film with FWHM of 2.35° and Simon Fichtner *et al.* [25] reported an $Al_{0.73}Sc_{0.27}N$ thin film with FWHM of 1.83°. Co-sputtering with two targets and sputtering process using alloy target is used respectively. Our work provides comparable results on the AlScN thin film quality with similar concentrations. In addition, the optimized film has a very low amount of AOGs. When the film is thicker, the AOGs grow further, making the crystalline quality deteriorate further. Therefore, it is necessary to start a recipe with minimal AOGs and then tune the thickness and stress.

Authorized licensed use limited to: ShanghaiTech University. Downloaded on June 26,2022 at 07:31:59 UTC from IEEE Xplore. Restrictions apply.

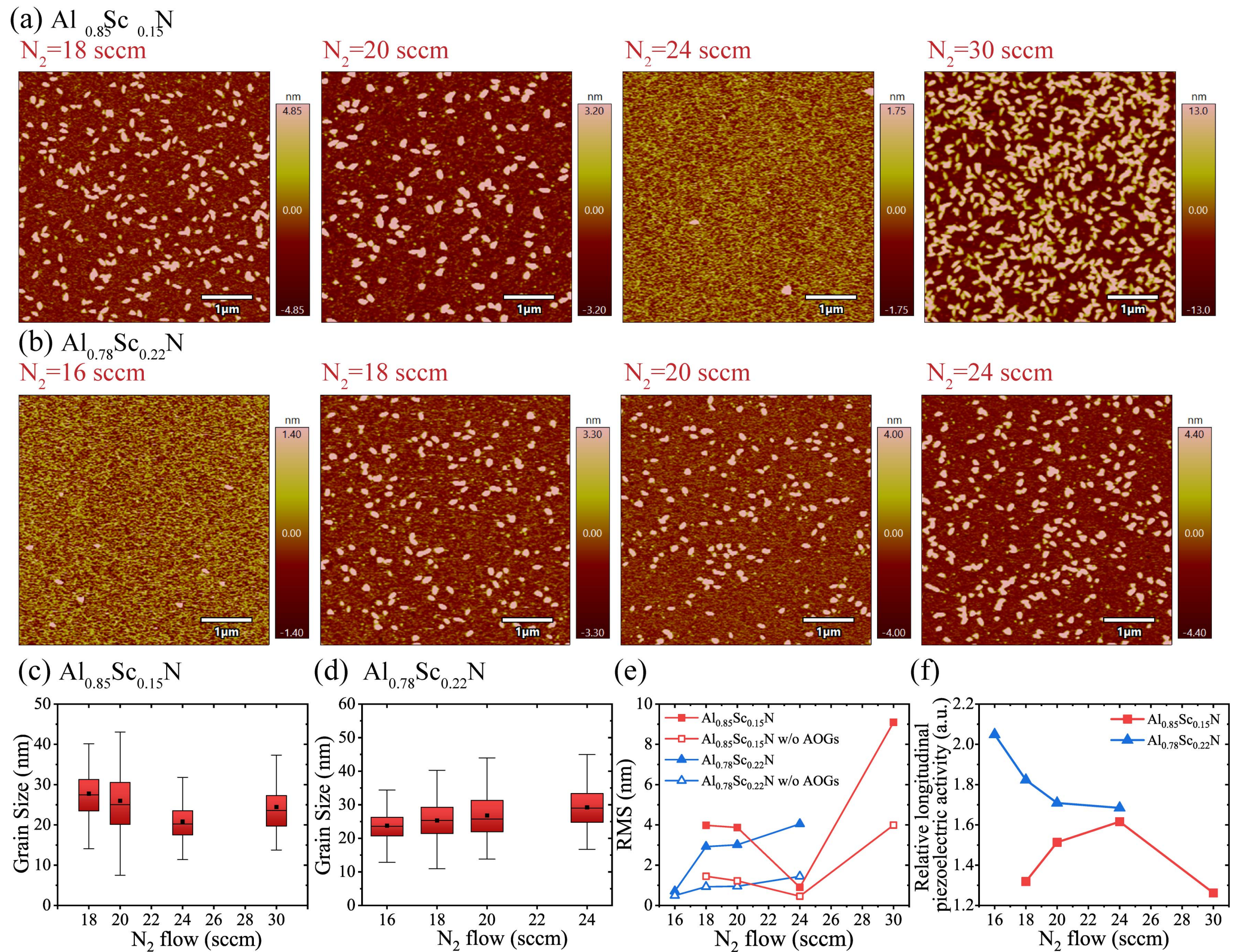

Fig. 5. AFM images of AlScN with different N_2 flow, (a) $Al_{0.85}Sc_{0.15}N$, (b) $Al_{0.78}Sc_{0.22}N$. revise Grain size of (c) $Al_{0.85}Sc_{0.15}N$, (d) $Al_{0.78}Sc_{0.22}N$ as function of N_2 flow. (e) The influence of the abnormal orientation grains on roughness. (f) Relationship between relative longitudinal piezoelectric constant and N_2 flow.

With the Bragg equation, the lattice constant c can be calculated using the position of the peak in the XRD pattern. As shown in Figure 4c, the lattice constant c of AlScN can be affected by more than just the doping concentration. This is the first report on the effect of process pressure on the lattice constant in sputtering. In $Al_{0.78}Sc_{0.22}N$, the lattice constant c decreases from 4.994 Å to 4.979 Å as the N_2 flow increases from 16 sccm to 24 sccm. At the same N_2 flow, c of $Al_{0.78}Sc_{0.22}N$ is smaller than for $Al_{0.85}Sc_{0.15}N$, which is the same as the results reported for the other works [43], [44]. The N_2 flow rate as a function of pressure in the chamber is given in Figure 4d.

Figures 5a and b show the AFM surface morphology with $Al_{0.85}Sc_{0.15}N$ and $Al_{0.78}Sc_{0.22}N$. Compared to SEM images, AFM morphology is more conducive to the judgment of grain quantity and size. A large number of abnormally oriented grains can be observed on the surface of the film. The increase of abnormally oriented grains in the film results in the decrease of k_t^2 [47]. In $Al_{0.85}Sc_{0.15}N$, the height range was 26 nm at worst and 3.5 nm at best, indicating that the size of abnormally oriented grains also changed with the change of pressure. Abnormally oriented grains account for up to 60% of the surface area of the film, and these grains have no piezoelectric response, which could have a serious negative impact on device performance. As shown in Figures 5c and d, the grain size of the films at the two concentrations ranges from 10 nm to 40 nm which obtained by AFM characterization. The results indicate pressure affects grain size and follows the same trend as FWHM and AOGs. The AFM Roughness statistics in RMS (R_{rms}) are shown in Figure 5e. In the group of $Al_{0.85}Sc_{0.15}N$, the trend of the R_{rms} is coincidental with the FWHM XRD of the AlScN (with AOGs). From the SEM picture, we could conclude that the main contribution of the R_{rms} is the AOGs. In each group of different Sc concentrations, the best FWHM XRD sample shows the lowest roughness.

The relative longitudinal piezoelectric constants under different N_2 flows are shown in Figure 5f. All measurement data are performed in PM300 and normalized to the pure AlN film piezoelectric constant of −6.6 pC/N. Combining Figures 4 and 5, it can be concluded that the relative

Authorized licensed use limited to: ShanghaiTech University. Downloaded on June 26,2022 at 07:31:59 UTC from IEEE Xplore. Restrictions apply.

longitudinal piezoelectric constant favors better XRD FWHM and less AOGs density, i.e., the 500 nm $Al_{0.85}Sc_{0.15}N$ and $Al_{0.78}Sc_{0.22}N$ achieves the optimal value of 1.6 (−9.8 pC/N) and 2.1 (−12.8 pC/N), respectively. The piezoelectric constants exhibit a correlated trend as XRD FWHM versus N_2 flow, which can be used as a criterion for the piezoelectric constant evaluation. In the case of $Al_{0.85}Sc_{0.15}N$ films with more AOGs have a relatively lower piezoelectric constant.

The SEM, XRD, AFM and piezoelectric results of $Al_{0.85}Sc_{0.15}N$ and $Al_{0.78}Sc_{0.22}N$ indicate that lower process pressure leads to better crystalline quality and thus higher piezoelectric coefficient. Thanks to the long mean free path, less collision happened during the sputtering and finally caused higher kinetic energy. With the N_2 flow increasing from 18 to 30 sccm, the number of abnormally oriented grains on the surface of the film first decreased and then increased. A clean AlScN surface was obtained at $N_2 = 24$ sccm, which was also shown in the rocking curve. At $N_2 = 24$ sccm, the optimum FWHM of 1.75° was obtained. This implies that there is an optimal ion bombardment energy during AlScN film deposition, and an excessive increase in energy can instead lead to the deterioration of crystal quality. As shown in Figure 4b, the FWHM of 0002 $Al_{0.78}Sc_{0.22}N$ rocking curve in the center decreases from 2.24° to 1.95° with the increase of gas flow and reduction in the number of abnormally oriented grains, which represents the improvement of thin film quality. In contrast, only the crystalline quality improvement process was observed with the increase of ion flux energy in $Al_{0.85}Sc_{0.15}N$ film. The lower gas flow rate makes ignition difficultly and sputtering unstable, so the film is not successfully obtained. It is worth noting that the optimal c-axis orientation and the minimum number of abnormally oriented grains were obtained simultaneously. Although at $Al_{0.78}Sc_{0.22}N$, the crystalline quality gets better as the process pressure decreases, no optimal gas flow was found. However, compared with the film concentration of 15%, the optimal crystalline quality was not obtained at $N_2 = 24$ sccm, as shown in Figure 4a. Therefore, it can be proved that higher concentration films require higher plasma energy, which means lower chamber pressure.

Combined with the AFM height and grain size, we believe the basal plane is better aligned to the substrate normal direction, which results in a higher piezoelectric coefficient. Furthermore, a desired sputtering condition to achieve good crystalline quality may differ between different Sc concentrations. The higher Sc concentrations need a higher vacuum lever (higher kinetic energy) to achieve good quality. This has not been reported by other literature so far. By comparing the SEM/XRD/piezoelectric property results, we found that the XRD rocking curve has a strong correlation with the film piezoelectric constant compared to the AOGs conditions. However, the optimized deposition parameters, i.e. the N_2 flow, also bring a side effect on the stress, which could lead to the shift of film XRD peak location.

The influence of changing process pressure on the crystalline quality and piezoelectric properties of AlScN thin films during sputtering was analyzed to evaluate the limitations of controlling the stress of thin films by adjusting gas. The suspension structure of RF resonators, PMUT and piezoelectric sensors require the sputtering process to grow AlN thin films with controlled stress and vertical gradient. Otherwise, the structure can bend or even break [48], [49]. The stress range then determines the production yield. Both the average stress and stress range need to be controlled. At present, the main method to control the stress is to adjust the ion bombardment intensity by changing the gas in co-sputtering systems [25], [28], [50]. However, the number of abnormally oriented grains, crystalline quality and stress of thin films are all affected by the intensity of ions bombardment.

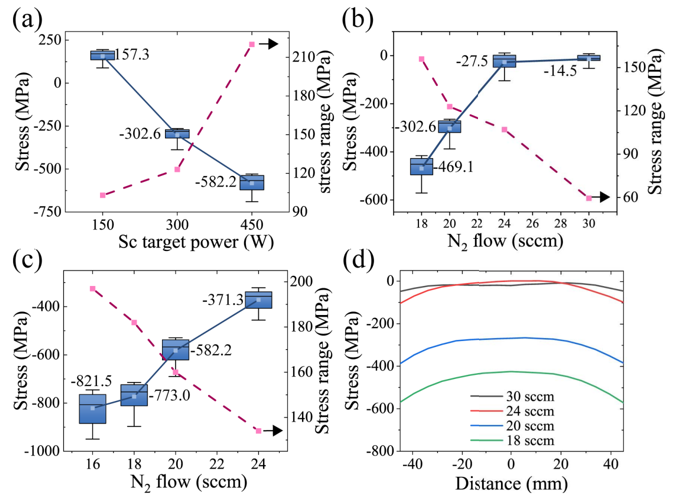

Fig. 6. (a) Stress of sputtered AlScN thin film as a function of Sc target for 20 sccm N_2 Stress of sputtered AlScN thin film as a function of the N_2 flow. Power of Sc target are (b) 300 W and (c) 450 W. (d) Stress distribution along wafer diameter at scandium target power of 300 W.

In Figures 6a-c, the stress of the 4-inch area is shown from the 8-inch wafer. N_2 flow rate changed from 16 sccm to 30 sccm, with a subsequent linear increase in pressure of chamber from 6×10^{-4} to 1.3×10^{-3} mbar. In Figure 6a, the average stress for $N_2 = 20$ sccm decreases from 157.3 MPa to −582.2 MPa with Sc target power increase from 150 W to 450 W. The range of stress was degraded. As a result, stress control is more difficult for higher Sc concentration films. As shown in Figure 6b, when the Sc concentration of AlScN thin films was 15%, the average value of the stress changes to the compressive with the increase of N_2 flow. N_2 flow increased from 18 to 30 sccm, and the average stress raised from −469.1 MPa to −14.5 MPa. Meanwhile, the stress range is gradually reduced from 156 MPa to 59 MPa. The stress range is more conducive to the manufacturing of thin film devices. As shown in Figure 6c, the average stress obtained at the same flow rate was more tensile due to the increase in the total power with $Al_{0.78}Sc_{0.22}N$. The N_2 flow increased from 16 to 24 sccm, and the stress range decreased from 197 MPa to 134 MPa. As shown in Figure 6d, in the co-sputtering system, the tilted mounting of the two targets over the substrate causes the AlScN thin film to form a flat stress region at the center of the wafer. Changes in stress are more obvious at the edge of the wafer. The intensity of ion bombardment is very inhomogeneous at low chamber pressures. The control of the ion flow is worse at the edges. From the above data, excellent average stress and ranges were

Authorized licensed use limited to: ShanghaiTech University. Downloaded on June 26,2022 at 07:31:59 UTC from IEEE Xplore. Restrictions apply.

obtained for the $Al_{0.85}Sc_{0.15}N$ thin films. However, this work found that the method has certain limitations in crystalline quality.

A few works have demonstrated stress control on sputtered AlScN thin films [25], [51]. The mixture proportion can cause a stress range over 1 GPa from compressive to tensile. Chamber pressure is a common method of linearly adjusting stress. However, as shown in Figure 4, the trend of crystalline quality with flow rate is not the same as the stress. For the $Al_{0.78}Sc_{0.22}N$ thin film, N_2 = 16 sccm shows a better crystalline quality. The average stress reached −821.5 MPa. The large stress can cause the suspended film to crack. In addition, the properly packed grains make AOGs more difficult to grow, which can be correlated with the in-line FWHM data [52]. By comparing the AOGs of $Al_{0.85}Sc_{0.15}N$ at N_2 = 30 sccm and N_2 = 18 sccm, it can be seen that tensile stress films are easier to grow abnormally oriented. Low energy and loose grain arrangement intensify Sc accumulation among the grain boundaries. In summary, the stress tuning by N_2 flows and pressure requires consideration of the effect on crystalline quality in the co-sputtering process.

IV. AlScN Thin Film ICP Etch

Anisotropic etching is required to define the reflection boundary and release window of the device. However, the etch rate decreases significantly with increasing Sc concentration, causing severe deterioration of both selectivity and sidewall profile. Therefore, dry etching of highly doped AlScN needs to be developed as a necessary process for suspension structures. Figure 7a shows the etch rate, profile and selectivity related to Cl_2 flow rate at 550 W ICP power, 200 W RF power, BCl_3/N_2 = 30/20 sccm, pressure = 5 Pa. Cl_2 is the main reactive etching gas, which enhances the etching anisotropy. As the Cl_2 flow rate increases from 15 sccm to 30 sccm, the profile slowly increases from 70° to approximately 73°. However, for the selectivity and etching rate, the increase of Cl_2 gas has no obvious effect on them. The etching rate was about 65 nm/min, however, the best etching selectivity ratio of 0.55 is achieved at 25 sccm due to the saturation of plasma energy. Therefore, maintaining a Cl_2 flow rate of 25 sccm and further increasing the RF power can improve the etch rate.

Figure 7b shows the relationship of etching rate, profile and selectivity as a function of RF bias power at ICP power = 550 W and $Cl_2/BCl_3/N_2$ = 25/30/20 sccm. When RF power increases from 200 W to 350 W, both the etching rate and selectivity increase significantly. The etching rate increases from ∼70 nm/min to ∼130 nm/min and the selectivity increases from 0.55 to approximately 0.8. This is because the energy of the plasma increases as the RF power is increased. Moreover, the nonvolatile etching process product $ScCl_3$ could cover the etched surface, making it difficult for the Cl_2 gas to react with the AlScN film. Higher plasma energy results in the more physical bombardment of the etched surface by heavier particles, which helps strip $ScCl_3$ from the surface and expose AlScN, indirectly promoting the chemical reaction rate. The silicon oxide hard mask can only be reacted by physical bombardment. Therefore, both selectivity and etching rate show an increase versus RF power. However, the etching rate almost reached saturation when the RF power exceeded 350 W. In addition, the selectivity drops to about 0.6, which could attribute to the physical bombardment being too strong, making the consumption of the mask increase. For the profile, the angle fluctuates between 70° and 77° with the increase of RF power. Since the RF power is larger, the anisotropy of etching is stronger and the angles are more vertical. As shown in Figure 7c, the best profile of 77° was obtained at an RF power of 350 W. The SEM image of a Lamb-wave resonator design is shown in Figure 7d. No film crack is observed after device release. Depending on the device design, thicker AlScN film requires thicker SiO_2 hard masks, and the selectivity and sidewall profile optimization of PR/mask and mask/AlScN are more challenging.

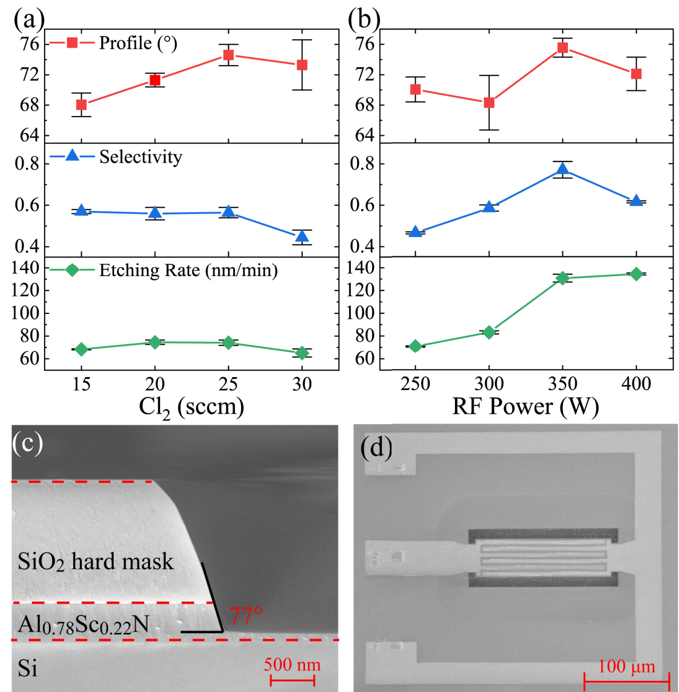

Fig. 7. (a) The etch rate, profile and selectivity related to Cl_2 flow rate at 550 W ICP power, 200 W RF power, BCl_3/N_2 = 30/20 sccm, pressure = 5 Pa. (b) schematic diagram of etching rate, profile and selectivity with RF power at 550 W ICP power, $Cl_2/BCl_3/N_2$ = 25/30/20 sccm. (c) SEM image of ICP etch profile for $Al_{0.78}Sc_{0.22}N$ film. (d) SEM of the Lamb-wave resonator with floating bottom electrode.

V. Result

As shown in Figure 8a, the devices were fabricated by a three-layer mask process. The thicknesses of the Platinum (Pt) bottom electrode and the Aluminum (Al) top electrode were 100 nm and 200 nm, respectively. ICP etching used 2 μm SiO_2 as a hard mask to define the reflection boundary and release window of the device. Finally, XeF_2 isotropic etching was used to release the device.

Figures 8b and c show the measured admittance spectrum of the Lamb-wave resonator based on 500 nm $Al_{0.78}Sc_{0.22}N$ and $Al_{0.85}Sc_{0.15}N$ thin films, respectively. Considering the stress and quality of the films, flow rates of 24 sccm and 20 sccm were used for device fabrications of $Al_{0.85}Sc_{0.15}N$

Authorized licensed use limited to: ShanghaiTech University. Downloaded on June 26,2022 at 07:31:59 UTC from IEEE Xplore. Restrictions apply.

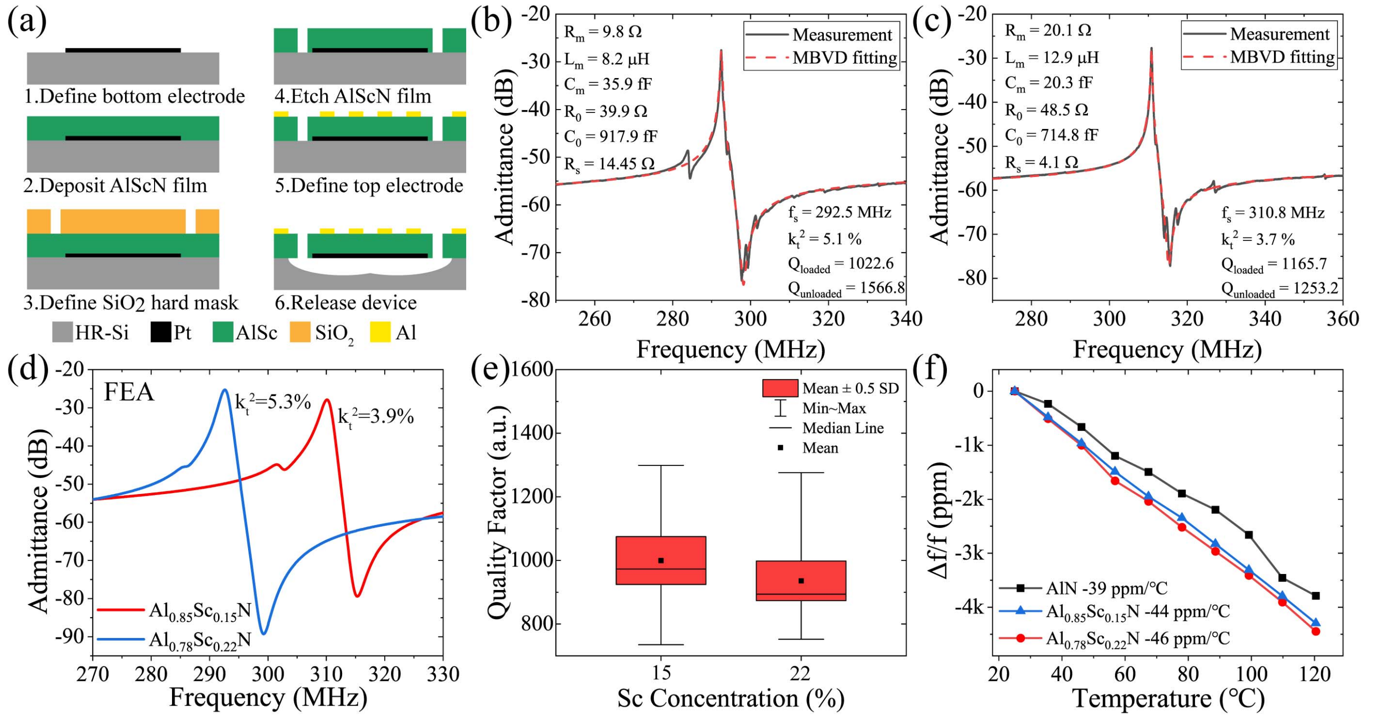

Fig. 8. (a) Fabrication process of Lamb-wave resonator. Measured admittance spectra of the Lamb-wave resonators with (b) $Al_{0.78}Sc_{0.22}N$, (c) $Al_{0.85}Sc_{0.15}N$ and their six equivalent circuit parameters of the MBVD model. (d) The FEA 2D simulation of S0 mode Lamb-wave resonator. (e) Measured quality factor distribution of $Al_{0.85}Sc_{0.15}N$ and $Al_{0.78}Sc_{0.22}N$ Lamb-wave resonator. (f) Temperature Coefficient of Frequency with pure AlN and $Al_{0.78}Sc_{0.22}N$.

TABLE III
GEOMETRIC DIMENSIONS OF THE LAMB-WAVE RESONATOR

Parameters	Value	Parameters	Value
IDT aperture	248 μm	AlScN thickness	500 nm
IDT electrode width	6 μm	Pt thickness	100 nm
IDT finger electrodes	6	Al thickness	200 nm

and $Al_{0.78}Sc_{0.22}N$, respectively. The device design parameters are shown in Table III. Both devices have the same 6 IDT finger electrodes. The k_t^2 of S0 mode Lamb-wave resonators are 5.1% and 3.7%. Compared with the 2.06% of pure AlN, the k_t^2 are improved by 80% and 152% with $Al_{0.85}Sc_{0.15}N$ and $Al_{0.78}Sc_{0.22}N$. The higher concentration of the film makes the frequency drop from 310.8 MHz to 292.5 MHz, which proves that the S0 mode phase velocity of the AlScN film decreases with the increase of the concentration. Using the material parameters in Table III, the results of the FEA 2D simulation are shown in Figure 8d, achieving a good fit with measurement. The static capacitor C_0 is changed from 917.9 fF to 714.8 fF showing that 22% has a higher permittivity than 15%. Figure 8e shows the measured quality factor distribution for the 15% and 22% concentrations. Both have similar maximum and minimum quality factors. The mean quality factor (999.6) of $Al_{0.85}Sc_{0.15}N$ is slightly higher than that of $Al_{0.78}Sc_{0.22}N$ (935.9). Figure 8f shows the temperature coefficient of frequency measurements using devices with pure AlN and $Al_{0.78}Sc_{0.22}N$. The temperature increases from 25 °C to 120 °C and both AlN and $Al_{0.78}Sc_{0.22}N$ devices exhibit a linear frequency change, proving that mainly the first order temperature coefficient dominates. The difference in temperature coefficient of the doped AlN decreases from −39 ppm/°C to −46 ppm/°C.

VI. CONCLUSION

In this article, we have demonstrated optimized AlScN co-sputtering and etching processes. High scandium concentrations of the AlScN thin films require more plasma energy during grain growth, which can be achieved by reducing N_2 gas flow rate to increase the energy obtained from plasma. However, the N_2 flow rate in turn affects the stress. The balance between crystalline quality and stress needs to be considered when selecting the flow rate. In addition, inappropriate energy could lead to Sc accumulation with an increase in the number of abnormal orientation grains. The XRD FWHM of AlScN can be used directly to evaluate the piezoelectric constants. By optimizing the deposition condition, 500 nm $Al_{0.85}Sc_{0.15}N$ thin films with a FWHM of 1.75°, an average stress of −27.5 MPa and a stress range of 107 MPa over 4-inch area are obtained. The dry etching rate of AlScN could be significantly improved by increasing the RF power. An etching rate of 130 nm/min and a profile of 77° are achieved. Finally, Lamb-wave resonators have been fabricated based on $Al_{0.78}Sc_{0.22}N$ and $Al_{0.85}Sc_{0.15}N$ thin films, achieving a quality factor of over 1000, as well as 152% and 80% improvement in electromechanical coupling coefficients, compared to pure AlN thin film devices, respectively. The significant increase in electromechanical coupling coefficients brought by high quality and high Sc-doped AlScN demonstrates the great potential in RF applications.

Authorized licensed use limited to: ShanghaiTech University. Downloaded on June 26,2022 at 07:31:59 UTC from IEEE Xplore. Restrictions apply.

Acknowledgment

The authors appreciate the support from the ShanghaiTech Quantum Device Laboratory (SQDL) and the Analytical Instrumentation Center (SPST-AIC10112914) XRD Laboratory.

References

[1] Y. Qiu *et al.*, "Piezoelectric micromachined ultrasound transducer (PMUT) arrays for integrated sensing, actuation and imaging," *Sensors*, vol. 15, no. 4, pp. 8020–8041, 2015, doi: 10.3390/s150408020.

[2] Y. Lu *et al.*, "Ultrasonic fingerprint sensor using a piezoelectric micromachined ultrasonic transducer array integrated with complementary metal oxide semiconductor electronics," *Appl. Phys. Lett.*, vol. 106, no. 26, 2015, Art. no. 263503, doi: 10.1063/1.4922915.

[3] T. H. Ng and W. H. Liao, "Sensitivity analysis and energy harvesting for a self-powered piezoelectric sensor," *J. Intell. Mater. Syst. Struct.*, vol. 16, no. 10, pp. 785–797, Oct. 2005, doi: 10.1177/1045389x05053151.

[4] T. Wu, R. Lu, A. Gao, C. Tu, T. Manzaneque, and S. Gong, "A chip-scale RF MEMS gyrator via hybridizing lorentz-force and piezoelectric transductions," in *Proc. IEEE 32nd Int. Conf. Micro Electro Mech. Syst. (MEMS)*, Jan. 2019, pp. 887–890, doi: 10.1109/MEMSYS.2019.8870764.

[5] J. G. Andrews *et al.*, "What will 5G be?" *IEEE J. Sel. Areas Commun.*, vol. 32, no. 6, pp. 1065–1082, Jun. 2014, doi: 10.1109/JSAC.2014.2328098.

[6] R. C. Ruby, P. Bradley, Y. Oshmyansky, A. Chien, and J. D. Larson, "Thin film bulk wave acoustic resonators (FBAR) for wireless applications," in *Proc. IEEE Ultrason. Symp.*, Oct. 2001, pp. 813–821, doi: 10.1109/ULTSYM.2001.991846.

[7] R. C. Turner, P. A. Fuierer, R. E. Newnham, and T. R. Shrout, "Materials for high temperature acoustic and vibration sensors: A review," *Appl. Acoust.*, vol. 41, no. 4, pp. 299–324, 1994, doi: 10.1016/0003-682x(94)90091-4.

[8] S. Gong and G. Piazza, "Design and analysis of lithium-niobate-based high electromechanical coupling RF-MEMS resonators for wideband filtering," *IEEE Trans. Microw. Theory Techn.*, vol. 61, no. 1, pp. 403–414, Dec. 2013, doi: 10.1109/TMTT.2012.2228671.

[9] J. Zou, C.-M. Lin, A. Gao, and A. P. Pisano, "The multi-mode resonance in AlN Lamb wave resonators," *J. Microelectromech. Syst.*, vol. 27, no. 6, pp. 973–984, Dec. 2018, doi: 10.1109/jmems.2018.2867813.

[10] J. Zou and C. S. Lam, "Electrode design of AlN Lamb wave resonators," in *Proc. IEEE Int. Freq. Control Symp. (IFCS)*, May 2016, pp. 1–5, doi: 10.1109/FCS.2016.7563573.

[11] C. Cassella, Y. Hui, Z. Qian, G. Hummel, and M. Rinaldi, "Aluminum nitride cross-sectional Lamé mode resonators," *J. Microelectromech. Syst.*, vol. 25, no. 2, pp. 275–285, Apr. 2016, doi: 10.1109/JMEMS.2015.2512379.

[12] C. Cassella, N. Oliva, J. Soon, M. Srinivas, N. Singh, and G. Piazza, "Super high frequency aluminum nitride two-dimensional-mode resonators with k_t^2 exceeding 4.9%," *IEEE Microw. Wireless Compon. Lett.*, vol. 27, no. 2, pp. 105–107, Feb. 2017, doi: 10.1109/LMWC.2016.2646924.

[13] X. Zhao, L. Colombo, and C. Cassella, "Aluminum nitride two-dimensional-resonant-rods," *Appl. Phys. Lett.*, vol. 116, no. 14, Apr. 2020, Art. no. 143504, doi: 10.1063/5.0005203.

[14] M. Akiyama, T. Kamohara, K. Kano, A. Teshigahara, Y. Takeuchi, and N. Kawahara, "Enhancement of piezoelectric response in scandium aluminum nitride alloy thin films prepared by dual reactive cosputtering," *Adv. Mater.*, vol. 21, no. 5, pp. 593–596, Dec. 2008, doi: 10.1002/adma.200802611.

[15] M. Akiyama, K. Kano, and A. Teshigahara, "Influence of growth temperature and scandium concentration on piezoelectric response of scandium aluminum nitride alloy thin films," *Appl. Phys. Lett.*, vol. 95, no. 16, 2009, Art. no. 162107, doi: 10.1063/1.3251072.

[16] G. Esteves *et al.*, "$Al_{0.68}Sc_{0.32}N$ Lamb wave resonators with electromechanical coupling coefficients near 10.28%," *Appl. Phys. Lett.*, vol. 118, no. 17, Apr. 2021, Art. no. 171902, doi: 10.1063/5.0047647.

[17] X. Zhao, O. Kaya, M. Pirro, G. Michetti, L. Colombo, and C. Cassella, "An ultra-low impedance 4.8 GHz $Al_{72}Sc_{28}N$ resonant rods resonator with a record k_t^2 of 21.2%," in *IEEE MTT-S Int. Microw. Symp. Dig.*, Nov. 2021, pp. 312–315, doi: 10.1109/IMFW49589.2021.9642286.

[18] C. Höglund *et al.*, "Wurtzite structure $Sc_{1-x}Al_xN$ solid solution films grown by reactive magnetron sputter epitaxy: Structural characterization and first-principles calculations," *J. Appl. Phys.*, vol. 107, no. 12, 2010, Art. no. 123515, doi: 10.1063/1.3448235.

[19] A. Lozzi, E. Ting-Ta Yen, P. Muralt, and L. G. Villanueva, "$Al_{0.83}Sc_{0.17}N$ contour-mode resonators with electromechanical coupling in excess of 4.5%," *IEEE Trans. Ultrason., Ferroelectr., Freq. Control*, vol. 66, no. 1, pp. 146–153, Jan. 2019, doi: 10.1109/TUFFC.2018.2882073.

[20] K. Tonisch, V. Cimalla, C. Foerster, H. Romanus, O. Ambacher, and D. Dontsov, "Piezoelectric properties of polycrystalline AlN thin films for MEMS application," *Sens. Actuators A, Phys.*, vol. 132, no. 2, pp. 658–663, 2006, doi: 10.1016/j.sna.2006.03.001.

[21] M. Park, Z. Hao, R. Dargis, A. Clark, and A. Ansari, "Epitaxial aluminum scandium nitride super high frequency acoustic resonators," *J. Microelectromech. Syst.*, vol. 29, no. 4, pp. 490–498, Aug. 2020, doi: 10.1109/jmems.2020.3001233.

[22] M. Park, Z. Hao, D. G. Kim, A. Clark, R. Dargis, and A. Ansari, "A 10 GHz single-crystalline scandium-doped aluminum nitride Lamb-wave resonator," in *Proc. 20th Int. Conf. Solid-State Sensors, Actuat. Microsyst. Eurosensors XXXIII (TRANSDUCERS EUROSENSORS XXXIII)*, Jun. 2019, pp. 450–453, doi: 10.1109/transducers.2019.8808374.

[23] S. Leone *et al.*, "Metal-organic chemical vapor deposition of aluminum scandium nitride," *Phys. Status Solidi (RRL)–Rapid Res. Lett.*, vol. 14, no. 1, 2020, Art. no. 1900535, doi: 10.1002/pssr.201900535.

[24] Y. Lu *et al.*, "Surface morphology and microstructure of pulsed DC magnetron sputtered piezoelectric AlN and AlScN thin films," *Phys. Status Solidi (A)*, vol. 215, no. 9, Nov. 2017, Art. no. 1700559, doi: 10.1002/pssa.201700559.

[25] S. Fichtner, T. Reimer, S. Chemnitz, F. Lofink, and B. Wagner, "Stress controlled pulsed direct current co-sputtered $Al_{1-x}Sc_xN$ as piezoelectric phase for micromechanical sensor applications," *APL Mater.*, vol. 3, no. 11, 2015, Art. no. 116102, doi: 10.1063/1.4934756.

[26] Y. Lu *et al.*, "Elastic modulus and coefficient of thermal expansion of piezoelectric $Al_{1-x}Sc_xN$ (up to x = 0.41) thin films," *APL Mater.*, vol. 6, no. 7, Jul. 2018, Art. no. 076105, doi: 10.1063/1.5040190.

[27] S. Mertin *et al.*, "Non-destructive piezoelectric characterisation of sc doped aluminium nitride thin films at wafer level," in *Proc. IEEE Int. Ultrason. Symp. (IUS)*, Oct. 2019, pp. 2592–2595, doi: 10.1109/ULTSYM.2019.8925964.

[28] M.-A. Dubois and P. Muralt, "Stress and piezoelectric properties of aluminum nitride thin films deposited onto metal electrodes by pulsed direct current reactive sputtering," *J. Appl. Phys.*, vol. 89, no. 11, pp. 6389–6395, 2001, doi: 10.1063/1.1359162.

[29] A. Iqbal and F. Mohd-Yasin, "Reactive sputtering of aluminum nitride (002) thin films for piezoelectric applications: A review," *Sensors*, vol. 18, no. 6, p. 1797, Jun. 2018, doi: 10.3390/s18061797.

[30] P. Soussan, K. O'Donnell, J. D'Haen, G. Vanhoyland, E. Beyne, and H. A. C. Tilmans, "Pulsed DC sputtered aluminum nitride: A novel approach to control stress and C-axis orientation," in *Proc. Symp. G-Mater., Integr., Packag. Issues High-Freq. Devices II*, vol. 833. Warrendale, PA, USA: Online Proceedings Library, 2004, p. G1.5, doi: 10.1557/PROC-833-G2.2.

[31] S. Rassay, F. Hakim, C. Li, C. Forgey, N. Choudhary, and R. Tabrizian, "A segmented-target sputtering process for growth of Sub-50 nm ferroelectric scandium–aluminum–nitride films with composition and stress tuning," *Phys. Status Solidi (RRL)–Rapid Res. Lett.*, vol. 15, no. 5, 2021, Art. no. 2100087, doi: 10.1002/pssr.202100087.

[32] M. David Henry, T. R. Young, and B. Griffin, "ScAlN etch mask for highly selective silicon etching," *J. Vac. Sci. Technol. B, Microelectron.*, vol. 35, no. 5, Sep. 2017, Art. no. 052001, doi: 10.1116/1.4994841.

[33] R. James, Y. Pilloux, and H. Hegde, "Reactive ion beam etching of piezoelectric ScAlN for bulk acoustic wave device applications," in *Proc. 18th Int. Conf. Micro Nanotechnol. Power Gener. Energy Convers. Appl.*, vol. 1407, 2019, Art. no. 012083, doi: 10.1088/1742-6596/1407/1/012083.

[34] C.-M. Lin, V. Yantchev, J. Zou, Y.-Y. Chen, and A. P. Pisano, "Micromachined one-port aluminum nitride Lamb wave resonators utilizing the lowest-order symmetric mode," *J. Microelectromech. Syst.*, vol. 23, no. 1, pp. 78–91, Feb. 2014, doi: 10.1109/jmems.2013.2290793.

[35] D. F. Urban, O. Ambacher, and C. Elsässer, "First-principles calculation of electroacoustic properties of Wurtzite (Al,Sc)N," *Phys. Rev. B, Condens. Matter*, vol. 103, no. 11, Mar. 2021, Art. no. 115204, doi: 10.1103/physrevb.103.115204.

[36] A. Konno *et al.*, "ScAlN Lamb wave resonator in GHz range released by XeF_2 etching," in *Proc. IEEE Int. Ultrason. Symp. (IUS)*, Jul. 2013, pp. 1378–1381, doi: 10.1109/ULTSYM.2013.0350.

[37] J. Wang, M. Park, S. Mertin, T. Pensala, F. Ayazi, and A. Ansari, "A film bulk acoustic resonator based on ferroelectric aluminum scandium nitride films," *J. Microelectromech. Syst.*, vol. 29, no. 5, pp. 741–747, Oct. 2020, doi: 10.1109/jmems.2020.3014584.

Authorized licensed use limited to: ShanghaiTech University. Downloaded on June 26,2022 at 07:31:59 UTC from IEEE Xplore. Restrictions apply.

[38] M. Park, J. Wang, and A. Ansari, "High-overtone thin film ferroelectric AlScN-on-silicon composite resonators," *IEEE Electron Device Lett.*, vol. 42, no. 6, pp. 911–914, Jun. 2021, doi: 10.1109/LED.2021.3070274.
[39] N. Wang *et al.*, "Over 10% of k_{eff}^2 demonstrated by 2-GHz spurious mode-free $Sc_{0.12}Al_{0.88}N$ laterally coupled alternating thickness mode resonators," *IEEE Electron Device Lett.*, vol. 40, no. 6, pp. 957–960, Jun. 2019, doi: 10.1109/LED.2019.2910836.
[40] N. Wang, Y. Zhu, B. Chen, and Y. Zhang, "Over 12% of coupling coefficient demonstrated by 3 GHz $Sc_{0.12}Al_{0.88}N$ based laterally coupled alternating thickness (LCAT) mode resonators," in *Proc. IEEE Int. Ultrason. Symp. (IUS)*, Oct. 2019, pp. 1971–1973, doi: 10.1109/ULTSYM.2019.8926087.
[41] L. Colombo, A. Kochhar, C. Xu, G. Piazza, S. Mishin, and Y. Oshmyansky, "Investigation of 20% scandium-doped aluminum nitride films for MEMS laterally vibrating resonators," in *Proc. IEEE Int. Ultrason. Symp. (IUS)*, Sep. 2017, pp. 1–4, doi: 10.1109/ULTSYM.2017.8092076.
[42] S. Shao, Z. Luo, and T. Wu, "Optimization of S1 Lamb wave resonators with $A_{10.8}Sc_{0.2}N$," in *Proc. IEEE 16th Int. Conf. Nano/Micro Engineered Mol. Syst. (NEMS)*, Apr. 2021, pp. 1523–1526, doi: 10.1109/NEMS51815.2021.9451451.
[43] N. Kurz *et al.*, "Experimental determination of the electro-acoustic properties of thin film AlScN using surface acoustic wave resonators," *J. Appl. Phys.*, vol. 126, no. 7, Aug. 2019, Art. no. 075106, doi: 10.1063/1.5094611.
[44] M. A. Caro *et al.*, "Piezoelectric coefficients and spontaneous polarization of ScAlN," *J. Phys. Condens. Matter*, vol. 27, no. 24, 2015, Art. no. 245901, doi: 10.1088/0953-8984/27/24/245901.
[45] Y. Zheng, M. Park, A. Ansari, C. Yuan, and S. Graham, "Self-heating and quality factor: Thermal challenges in aluminum scandium nitride bulk acoustic wave resonators," in *Proc. 21st Int. Conf. Solid-State Sens., Actuators Microsyst. (Transducers)*, Jun. 2021, pp. 321–324, doi: 10.1109/TRANSDUCERS50396.2021.9495613.
[46] S. Rassay, D. Mo, C. Li, N. Choudhary, C. Forgey, and R. Tabrizian, "Intrinsically switchable ferroelectric scandium aluminum nitride Lamb-mode resonators," *IEEE Electron Device Lett.*, vol. 42, no. 7, pp. 1065–1068, Jul. 2021, doi: 10.1109/LED.2021.3078444.
[47] C. Liu, B. Chen, M. Li, Y. Zhu, and N. Wang, "Evaluation of the impact of abnormally orientated grains on the performance of ScAlN-based laterally coupled alternating thickness (LCAT) mode resonators and Lamb wave mode resonators," in *Proc. IEEE Int. Ultrason. Symp. (IUS)*, Sep. 2020, pp. 1–3, doi: 10.1109/IUS46767.2020.9251507.
[48] G. Piazza, P. J. Stephanou, and A. P. Pisano, "Piezoelectric aluminum nitride vibrating contour-mode MEMS resonators," *J. Microelectromech. Syst.*, vol. 15, no. 6, pp. 1406–1418, Dec. 2006, doi: 10.1109/jmems.2006.886012.
[49] M. Park and A. Ansari, "Epitaxial $Al_{0.77}Sc_{0.23}N$ SAW and Lamb wave resonators," in *Proc. Joint Conf. IEEE Int. Freq. Control Symp. Int. Symp. Appl. Ferroelectr. (IFCS-ISAF)*, Jul. 2020, pp. 1–3, doi: 10.1109/IFCS-ISAF41089.2020.9234850.
[50] S. Barth *et al.*, "Sputter deposition of stress-controlled piezoelectric AlN and AlScN films for ultrasonic and energy harvesting applications," *IEEE Trans. Ultrason., Ferroelectr., Freq. Control*, vol. 61, no. 8, pp. 1329–1334, Aug. 2014, doi: 10.1109/TUFFC.2014.3040.
[51] S. Mishin and Y. Oshmyansky, "Stress control for highly doped aluminum scandium nitride films," in *Proc. IEEE Int. Ultrason. Symp. (IUS)*, Oct. 2018, pp. 1–9, doi: 10.1109/ULTSYM.2018.8579889.
[52] C. S. Sandu *et al.*, "Abnormal grain growth in AlScN thin films induced by complexion formation at crystallite interfaces," *Phys. Status Solidi (A)*, vol. 216, no. 2, Jan. 2019, Art. no. 1800569, doi: 10.1002/pssa.201800569.

Shuai Shao received the B.S. degree in electrical engineering from Xidian University, Xi'an, China, in 2018. He is currently pursuing the Ph.D. degree with ShanghaiTech University, Shanghai, China.

His research interest includes design and microfabrication techniques of MEMS resonators for radio frequency microsystems.

Zhifang Luo (Student Member, IEEE) received the B.S. degree in physics from ShanghaiTech University, Shanghai, China, in 2019, where he is currently pursuing the Ph.D. degree in electrical engineering.

His research interests include the design and microfabrication techniques of piezoelectric microelectromechanical system (MEMS) resonators for RF and sensing applications and hybrid microsystems based on the integration of MEMS device with photonics for signal processing.

Yuan Lu received the Ph.D. degree in microsystem engineering from the University of Freiburg, Germany, with a dissertation on the magnetron sputtered AlN/AlScN for electro-acoustic applications, which was done at the Fraunhofer Institute for Applied Solid State Physics. Later, he joined Evatec, Shanghai Branch, where has been working as a Technical Marketing Manager since 2020, focusing on technical solutions and marketing research for the semiconductor customers in China and also contributing in new hardware and process covering emerging material and device applications.

Andrea Mazzalai was born in Trento, Italy, in 1983. He received the master's degree (Hons.) in physics of matter from the University of Trento in 2008 and the Ph.D. degree from the Institute of Material Science, École Polytechnique Fédérale de Lausanne (EPFL), in 2014, with a thesis focusing on PVD deposition of PZT for MEMS applications and energy harvesting. He has served EPFL as a Post-Doctoral Researcher in 2015. Then, he joined Metallux SA as a Product Engineer in the field of hybrid circuits sensors for automotive and medical applications until 2017. After three years as a Scientist at Evatec AG, he has been leading the process engineering group focusing on piezoelectric materials and related electrodes since 2020.

Carlo Tosi received the Ph.D. degree in materials science and engineering from the University of Florence, Italy, with a dissertation on thin film semiconductor radiation detectors for high energy physics application in collaboration with the Italian National Institute of Nuclear Physics and CERN Geneva. He worked both in academy, as a Researcher in the same field and in industry, as a Technology Manager, with large multinational companies, such as General Electric, ABB, Alstom, and Oerlikon. In 2019, he joined Evatec AG, Switzerland, as a Product Marketing Manager, where he is successfully contributing to expand company's installed base and share within the cellular RF front end market. He has authored and coauthored a large number of publications in international scientific journals.

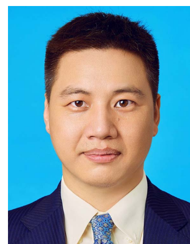

Tao Wu (Senior Member, IEEE) received the B.S. degree (Hons.) in electrical engineering from Zhejiang University, China, in 2007, and the M.S. and Ph.D. degrees from the University of California at Los Angeles, Los Angeles, CA, USA, in 2009 and 2011, respectively.

He was a Process TD Engineer with Intel Corporation, Hillsboro, OR, USA, from 2014 to 2015. Then, he was a Post-Doctoral Research Fellow with Stanford University and Northeastern University from 2014 to 2017. He is currently an Assistant Professor at the School of Information Science and Technology, ShanghaiTech University, Shanghai, China. He has authored or coauthors more than 60 papers in prestigious IEEE journals and conferences. His research interests include design and fabrication of multiferroic transducers, piezoelectric resonators, and integrated circuit for MEMS-based microsystems.

Authorized licensed use limited to: ShanghaiTech University. Downloaded on June 26,2022 at 07:31:59 UTC from IEEE Xplore. Restrictions apply.